*Inorg. Chem.* **2007**, *46*, 6556–6564


# A Spectroscopic and Computational Investigation of the Vanadomolybdate Local Structure in the Lyonsite Phase $Mg_{2.5}VMoO_8$

**Jared P. Smit,[†,§] Hack-Sung Kim,[†,‡,§] Ian Saratovsky,[†] Klaus B. Stark,[||] George Fitzgerald,[⊥] Gerry W. Zajac,[#] Jean-François Gaillard,*[,†] Kenneth R. Poeppelmeier,*[,†] and Peter C. Stair*[,†,‡]**

*Department of Chemistry, Northwestern University, 2145 Sheridan Road, Evanston, Illinois 60208, Chemistry Division, Argonne National Laboratory, 9700 South Cass Avenue, Argonne, Illinois 60439, Accelrys, Inc., 1042 Kress St., Houston, Texas 77020, Accelrys, Inc., 10188 Telesis Court, San Diego, California 92121, Ineos Technologies, 150 West Warrenville Road, Naperville, Illinois 60563, and Department of Environmental Engineering and Science, Northwestern University, 2145 Sheridan Road Evanston, Illinois 60208*

Received April 10, 2007

The vibrational spectrum of $Mg_{2.5}VMoO_8$ obtained by quantum mechanical simulation is compared with the experimentally observed Raman spectrum. This simulation suggests that the observed band at 1016 $cm^{-1}$ is attributed to the Mo═O–Mg stretching from two-coordinate oxygen atoms that are adjacent to $Mg^{2+}$ cation vacancies. Extended X-ray absorption fine structure spectroscopy supports the structural model used to simulate the vibrational modes in $Mg_{2.5}VMoO_8$ that match the observed Raman data.

## Introduction

Vibrational Raman spectroscopy has been applied to the characterization of solid-state inorganic oxides, and the assignment and interpretation of the Raman bands provides atomic-scale information on the structure of the materials that is complementary to X-ray diffraction. High-frequency Raman bands (>1000 $cm^{-1}$), in particular, those arising from supported metal oxides have long been attributed to the M═O (M = V, Mo, W) stretching vibrations, where oxygen atoms are one-coordinate.[1−3] For example, the Raman bands at 1034, 1012, and 1027 $cm^{-1}$ observed under dehydrated conditions have been assigned to surface terminal V═O, Mo═O, and W═O stretching vibrations, respectively.[4] These high-frequency vibrations red shift to 930, 975, and 990 $cm^{-1}$, respectively, under hydrous conditions.[4] The red shift has been attributed to bonding between M═O and water, which increases the coordination number of oxygen to two or more.[4]

Recent examinations of crystalline $Mg_{2.5}VMoO_8$[5,6] and $Mg_{2.5}VWO_8$[7] by Raman spectroscopy demonstrated that these materials exhibit bulk bands similar in frequency to surface M═O species.[7,8] High-frequency bands were observed at 1016 and 1035 $cm^{-1}$ in the Raman spectra of crystalline $Mg_{2.5}VMoO_8$ and $Mg_{2.5}VWO_8$ and were assigned to the molybdenum−oxo (Mo═O) bond and the tungsten−oxo (W═O) bond, respectively.[7] This result is remarkable because all oxygen atoms bonded to Mo and W in the crystalline $Mg_{2.5}VMoO_8$ and $Mg_{2.5}VWO_8$ bulk structures are at least two-coordinate. Although the high-frequency bands at 1016 and 1035 $cm^{-1}$ were attributed to two-coordinate oxygen atoms that border $Mg^{2+}$ cation vacancies in the

* To whom correspondence should be addressed. E-mail: jf-gaillard@northwestern.edu (J.-F.G.); krp@northwestern.edu (K.R.P.); pstair@northwestern.edu (P.C.S.).
† Department of Chemistry, Northwestern University.
‡ Chemistry Division, Argonne National Laboratory.
|| Accelrys, Inc., Houston, TX.
⊥ Accelrys, Inc., San Diego, CA.
# Ineos Technologies, Naperville, IL.
+ Department of Environmental Engineering and Science, Northwestern University.
§ Authors with equal contributions.

(1) Stencel, J. M.; Makovsky, L. E.; Diehl, J. R.; Sarkus, T. A. *J. Raman Spectrosc.* **1984**, *15*, 282−287.
(2) Desikan, A. N.; Huang, L.; Oyama, S. T. *J. Chem. Soc., Faraday Trans.* **1992**, *88*, 3357−3365.
(3) Oyama, S. T.; Went, G. T.; Lewis, K. B.; Bell, A. T.; Somorjai, G. A. *J. Phys. Chem.* **1989**, *93*, 6786−6790.
(4) Chan, S. S.; Wachs, I. E.; Murrell, L. L.; Wang, L.; Hall, W. K. *J. Phys. Chem.* **1984**, *88*, 5831−5835.
(5) Wang, X.; Stern, C. L.; Poeppelmeier, K. R. *J. Alloys Compd.* **1996**, *243*, 51−58.
(6) Zubkov, V. G.; Leonidov, I. A.; Poeppelmeier, K. R.; Kozhevnikov, V. L. *J. Solid State Chem.* **1994**, *111*, 197−201.
(7) Pless, J. D.; Kim, H.-S.; Smit, J. P.; Wang, X.; Stair, P. C.; Poeppelmeier, K. R. *Inorg. Chem.* **2006**, *45*, 514−520.
(8) Smit, J. P.; Kim, H.-S.; Pless, J. D.; Stair, P. C.; Poeppelmeier, K. R. *Inorg. Chem.* **2006**, *45*, 521−528.



10.1021/ic7006815 CCC: $37.00 
Published on Web 07/13/2007

crystal framework, there was no direct evidence that the high-frequency Raman bands were produced by these structural features.

In the current work, the vibrational spectrum of $Mg_{2.5}VMoO_8$ obtained by quantum mechanical simulation is compared with the experimentally observed Raman spectrum. This simulation suggests that the observed band at 1016 $cm^{-1}$ is attributed to the Mo═O−Mg stretching from two-coordinate oxygen atoms that are adjacent to $Mg^{2+}$ cation vacancies, while also demonstrating the ability of the program to accurately treat large structures. Extended X-ray absorption fine structure (EXAFS) spectroscopy supports the structural model used to simulate the vibrational modes in $Mg_{2.5}VMoO_8$ that match the observed Raman data. Finally, this study demonstrates that one-coordinate oxygen atoms are not always required to give Raman bands at high frequencies (higher than ∼1000 $cm^{-1}$).

## Experimental Details

Polycrystalline $Mg_{2.5}VMoO_8$ was synthesized by the stoichiometric addition of MgO, $V_2O_5$, and $MoO_3$. The powder was heated in a platinum crucible at 1100 °C for 24 h. Phase purity was confirmed by powder X-ray diffraction. Powder X-ray diffraction patterns were measured in air at room temperature on a Rigaku diffractometer (Cu Kα radiation with Ni filter, 40 kV, 20 mA, $2\theta = 10-70°$, 0.05° step, 1 s count time). The Raman spectrum (100−1200 $cm^{-1}$) of polycrystalline $Mg_{2.5}VMoO_8$ was collected on a Bio-Rad FT-Raman spectrometer with 0.5 $cm^{-1}$ resolution. Two hundred scans were averaged to improve the signal-to-noise ratio.

**Computational Details.** All calculations were performed using the density functional theory (DFT) program DMol$^3$ provided by Accelrys Inc.[9,10] DMol$^3$ is available as part of Materials Studio by Accelrys Inc. DMol$^3$ uses a basis set of numeric atomic functions, which are exact solutions to the Kohn−Sham equations for the atoms.[11] These basis sets are generally more complete than a comparable set of linearly independent Gaussian functions and have been demonstrated to have small basis set superposition errors.[11] In the present study, a polarized split valence basis set, termed the double numeric polarized (DNP) basis set has been used. All calculations have been performed using the nonlocal PBE functional.[12]

Atom-centered grids were used for the numerical integration. The particular grid used about 1000 grid points for each atom in the calculation and corresponds to the "Medium" option in DMol$^3$ (*Materials Studio DMol$^3$*, version 4.0; Accelrys Inc.: San Diego, CA). A real space cutoff of 4.4 Å was used for the numerical integration. All SCF calculations were converged to a root-mean-square change in the charge density of less than $1 \times 10^{-5}$ Hartree (Ha). Sets of $2 \times 4 \times 1$ and $2 \times 2 \times 1$ symmetrized k-points were used for the smaller model (model I, see below) and the larger models (models II and III, see below), respectively. Geometries were optimized using analytic gradients and an efficient algorithm employing delocalized internal coordinates.[13] The atomic positions were optimized at experimental cell parameters so that the change of energy was less than $2 \times 10^{-5}$ Ha, and the change of the maximum force on the atoms was less than 0.004 Ha $Å^{-1}$. For the heavy-metal atoms DFT semicore pseudopotentials (DSPP) have been employed.[14] DSPPs replace the core electrons by a single effective potential, reducing the computational cost, and introduce scalar relativistic effects.

The optimized geometries vibrational spectra were calculated using a finite-differencing approximation. Since DMol$^3$ does not calculate Raman intensities, only the positions of the normal modes were obtained and identified by animation within the Materials Studio suite of software (*Materials Studio*, version 4.0; Accelrys Inc.: San Diego, CA).

**X-ray Absorption Spectroscopy.** $MgMoO_4$ and $Mg_3(VO_4)_2$ reference standards and $Mg_{2.5}VMoO_8$ were finely ground in ethanol, diluted with BN, cold pressed into pellets (Ø = 12 mm, 0.5 mm thick), and supported between two pieces of Kapton tape. Transmission spectra were collected at several different locations on each sample and reproducibility ensured sample homogeneity.

X-ray absorption spectra (XAS) were measured at DND-CAT (sector 5, beam line 5BMD) of the Advanced Photon Source at the V and Mo K-edges (5465 and 20 000 eV, respectively) in transmission. A Si(111) double-crystal monochromator was used to select wavelength. At the V K-edge, harmonics were eliminated with a flat Rh-coated mirror with a cutoff energy of 20 keV at 3 mrad and slight detuning (90% of $I_{0,max}$). At the Mo K-edge, the harmonics were eliminated with 70% detuning of $I_{0,max}$. For edge-energy calibration, the X-ray absorption spectra of reference Mo and V metal foils were measured with each sample. The metal foil edge energies were set to the first inflection points of their respective absorption edges determined by the first derivative and were set to 5465 eV for V and 20 000 eV for Mo. $MgMoO_4$ and $Mg_3(VO_4)_2$ were used as reference compounds. XAS spectra were measured in transmission geometry using Oxford ionization chambers with path lengths of 29.6 cm. Ionization chambers were filled with gas mixtures to obtain 10% absorption (15% $N_2$/85% He at the V K-edge, 75% $N_2$/25% Ar at the Mo K-edge) of the incident beam in $I_0$, 30% absorption (45% $N_2$/55% He at the V K-edge, 15% $N_2$/85% Ar at the Mo K-edge) in $I_T$ (sample), and 60% absorption (100% $N_2$ at the V K-edge, 80% $N_2$/20% Xe) in $I_{T2}$ (reference foils). $MgMoO_4$ and $Mg_3(VO_4)_2$ were mounted in an Oxford displex, and spectra were measured at 20, 100, 200, and 300 K. For each reference compound and $Mg_{2.5}VMoO_8$, sixteen replicate XAS spectra were collected to improve counting statistics.

A smooth atomic background was removed from each XAS spectrum, and the data were normalized to a step height of one. This is done so that $E_0$, the Fermi energy, can be consistently chosen as the first inflection point at the absorption edge step. $E_0$ is used by AutoBK[15,16] to determine the photoelectron wavenumber, $k = (2m(E - E_0)/\hbar^2)^{1/2}$, where $m$ is the electron mass, $\hbar$ is Planck's constant, and $E$ is the incident X-ray energy. This equation was used to convert the data from the measured EXAFS $\chi(E)$ to $\chi(k)$. The background function generated by the AutoBK algorithm[15,16] is made from third-order polynomial spline functions that are connected by knots. The background was removed from each data

(9) Delley, B. *J. Chem. Phys.* **1990**, *92*, 508−517.
(10) Delley, B. *J. Chem. Phys.* **2000**, *113*, 7756−7764.
(11) Delley, B. In *Density Functional Theory: A Tool for Chemistry*; Seminario, J. M., Politzer, P., Eds.; Elsevier: Amsterdam, The Netherlands, 1995.
(12) Perdew, J. P.; Burke, K.; Ernzerhof, M. *Phys. Rev. Lett.* **1996**, *77*, 3865−3868.
(13) Andzelm, J.; King-Smith, R. D.; Fitzgerald, G. *Chem. Phys. Lett.* **2001**, *335*, 321−326.
(14) Delley, B. *Phys. Rev. B: Condens. Matter Mater Phys.* **2002**, *66*, 155125/1−155125/9.
(15) Newville, M.; Livins, P.; Yacoby, Y.; Rehr, J. J.; Stern, E. A. *Jpn. J. App. Phys. Part 1* **1993**, *32*, 125−127.
(16) Ravel, B.; Newville, M.; Cross, J. O.; Bouldin, C. E. *Phys. B* **1995**, *209*, 145−147.

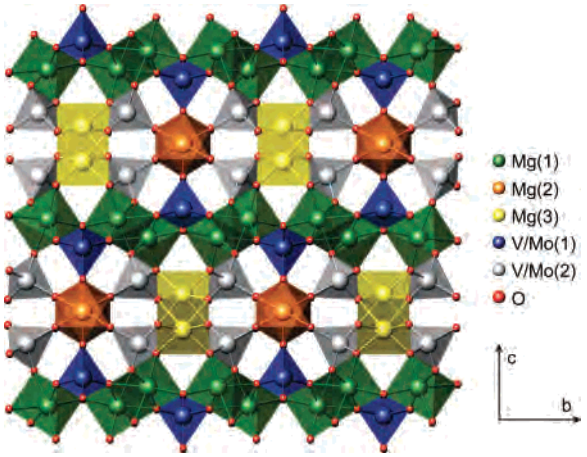


**Figure 1.** Structure of $Mg_{2.5}VMoO_8$.

set, and then the resulting $\chi(k)$ data (sixteen replicates) were averaged. Processing of all XAS data was performed using SixPack,[17] Athena,[18] and Artemis[18] graphical user interfaces for XAS processing built on IFEFFIT.[18−20] Data reduction and analysis were performed using the methods of Athena and Artemis.[18] The data were fit in *R* space with theoretical amplitudes and phases for single-scattering paths that were calculated from geometry-optimized model structures proposed for $Mg_{2.5}VMoO_8$ using the ab initio FEFF 6 code.[21] Fourier transforms of Mo and V K-edge $\chi(k)$ spectra were taken over similar photoelectron wavenumber ranges with the endpoints terminating at nodes, typically between $3.5 \leq k \leq 13.9$ Å$^{-1}$. A Kaiser−Bessel window function (d$k$ = 2) was used to dampen the EXAFS oscillations at endpoints. Least-squares fitting of theoretical phases and amplitudes to model compounds and $Mg_{2.5}VMoO_8$ were performed in Artemis.[18] Further analysis of the EXAFS spectra can be found in the Supporting Information.

## Results and Discussion

**Description of Structure.** $Mg_{2.5}VMoO_8$ adopts the lyonsite structure[22,23] and is depicted in Figure 1. The framework is built up from hexagonal tunnels created by $Mg(1)O_6$ octahedra and $Mg(3)O_6$ trigonal prisms. Crystallographically disordered vanadium- and molybdenum-centered tetrahedra line the tunnel wall and share corners with face-shared $Mg(2)O_6$ octahedra that form infinite columns passing through the center of the tunnels. The face-shared octahedra place $Mg^{2+}$ cations in close proximity, and on average, one out of every four magnesium atoms is missing to alleviate the Coulombic repulsions associated with cations in face-shared octahedra.

Because of the $Mg^{2+}$ cation vacancies, undercoordinated oxygen atoms are created. In a fully occupied model, all oxygen atoms are three-coordinate, bonded twice to $Mg^{2+}$ and once to either $V^{5+}$ or $Mo^{6+}$. When a cation vacancy occurs on a $Mg^{2+}$ site, some of the oxygen atoms become two-coordinate, bonded once to $Mg^{2+}$ and once to either $V^{5+}$ or $Mo^{6+}$, and the undercoordinated oxygen atoms displace toward the higher-valent transition metal cation to satisfy bond valence. This phenomenon is reflected in the crystallographic bond distances listed in Table 1, showing that both of the unique $V/MoO_4$ tetrahedra have one M−O bond length (1.716 and 1.713 Å, respectively) that is shorter than the other three (1.741−1.770 Å), corresponding to the displacement of the undercoordinated oxygen toward V/Mo. Because of the minimal difference in the M═O bond length between the two M═O−Mg bonds, the 1016 cm$^{-1}$ band corresponds to the presumed average of the two crystallographic positions. It is important to note that there are no singly bonded oxygen atoms in this model.

**Table 1.** Tetrahedral M−O Bond Lengths (Å) in the Crystallographic Model of $Mg_{2.5}VMoO_8$

| | |
|---|---|
| V/Mo(1)−O | 1.713(4) |
| | 1.741(3) |
| | 1.741(3) |
| | 1.770(5) |
| V/Mo(2)−O | 1.758(3) |
| | 1.716(3) |
| | 1.745(3) |
| | 1.744(3) |

No crystallographic order is observed by diffraction because of the isolated nature of the hexagonal tunnels that comprise the crystal framework.[5,24] The tetrahedral positions are occupied by 50% V and 50% Mo, and the face-shared octahedra are 75% occupied by Mg (25% unoccupied). Disordered tetrahedra should lead to two sets of Raman bands arising from both Mo−O−Mg and V−O−Mg in $Mg_{2.5}VMoO_8$. However, the Raman spectrum of $Mg_{2.5}VMoO_8$, seen in Figure 3, shows only one band above 1000 cm$^{-1}$ that was assigned to the stretching vibration of Mo−O−Mg that borders the cation vacancies.[7] The other band attributed to the V−O−Mg stretching vibration must appear below 1000 cm$^{-1}$ in the Raman spectrum of $Mg_{2.5}VMoO_8$. On the basis of the frequency−bond-order correlation,[25,26] the bond orders of V═O and Mo═O bonds bordering the cation vacancies were estimated to be 1.5−1.6 and 1.8−2.0, respectively.[8] Simulation of the vibrational Raman spectrum can potentially elucidate both whether the high-frequency bands are the result of the cation vacancies and also whether local order is present with respect to the disordered vanadium and molybdenum centered tetrahedral.

**Model Structures.** Three models were used to calculate the vibrational Raman spectrum. The first model (**I**) did not account for cation vacancies (denoted as □). In the other two models, every fourth magnesium atom along the infinite chains of face-shared octahedra was designated as a vacancy, creating magnesium trimers that are bordered by vacancies. Six tetrahedra surround each Mg or □ by sharing a corner.

(17) Webb, S. M. *Phys. Scr.* **2005**, *T115*, 1011−1014.
(18) Ravel, B.; Newville, M. *J. Synchrotron Radiat.* **2005**, *12*, 537−541.
(19) Newville, M. *J. Synchrotron Radiat.* **2001**, *8*, 96−100.
(20) Newville, M. *J. Synchrotron Radiat.* **2001**, *8*, 322−324.
(21) Rehr, J. J.; Zabinsky, S. I. *FEFF5: An ab initio multiple scattering XAFS Code*; Department of Physics, University of Washington: Seattle, WA, 1992; p 5.
(22) Hughes, J. M.; Starkey, S. J.; Malinconico, M. L.; Malinconico, L. L. *Am. Mineral.* **1987**, *72*, 1000−1005.
(23) Smit, J. P.; Stair, P. C.; Poeppelmeier, K. R. *Chem.−Eur. J.* **2006**, *12*, 5944−5953.
(24) Wang, X.; Pless, J. D.; Vander Griend, D. A.; Stair, P. C.; Poeppelmeier, K. R.; Hu, Z.; Jorgensen, J. D. *J. Alloys Compd.* **2004**, *379*, 87−94.
(25) Hardcastle, F. D.; Wachs, I. E. *J. Phys. Chem.* **1991**, *95*, 5031−5041.
(26) Hardcastle, F. D.; Wachs, I. E. *J. Raman Spectrosc.* **1990**, *21*, 683−691.

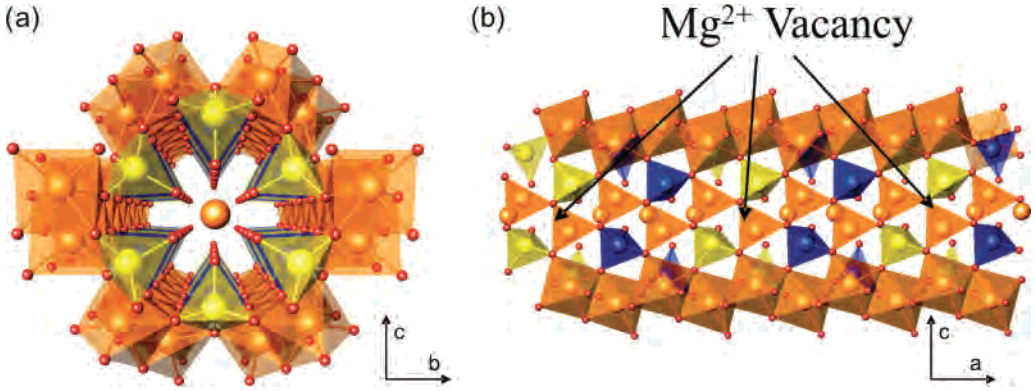


**Figure 2.** (a) Perspective view of the hexagonal tunnel showing the alternating nature of the $VO_4$ tetrahedra (blue) and $MoO_4$ tetrahedra (green). (b) View along the *a*-axis showing the Mg trimers and cation vacancies.

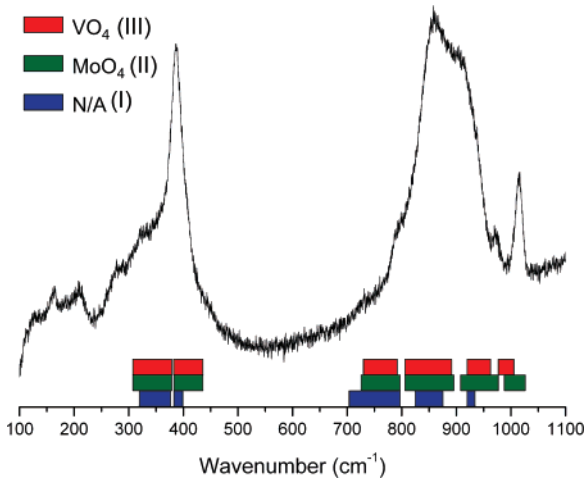


**Figure 3.** Vibrational Raman spectrum of $Mg_{2.5}VMoO_8$ with the calculated bands below. Because the calculated spectra do not have intensities, the bands are shown as ranges with identical height. Blue (N/A) is calculated without cation vacancies (**I**). Green ($MoO_4$) is calculated with $MoO_4$ tetrahedra around the cation vacancies (**II**). Red ($VO_4$) is calculated with $VO_4$ tetrahedra around the cation vacancies (**III**).

The six tetrahedra surrounding the vacancy were designated as $MoO_4$ in model (**II**), thereby causing the next six tetrahedra to be $VO_4$ to retain the correct stoichiometry. In this orientation, which has been described previously[8] and is depicted in Figure 2, the octahedra at the end of the magnesium trimer share corners with three $MoO_4$ and three $VO_4$ tetrahedra; the middle octahedron of the trimer shares corners with six $VO_4$ tetrahedra, and the vacancy is surrounded by six $MoO_4$ tetrahedra. For the final model (**III**), the $VO_4$ and $MoO_4$ tetrahedra were reversed.

The unit cell from the crystallographic model is not large enough to selectively remove one out of every four magnesium atoms along the face-shared infinite chain, and therefore, it is not large enough to selectively designate vanadium- and molybdenum-centered tetrahedra surrounding the vacancies. To obtain a unit cell with four magnesium atoms along the *a*-axis, it is necessary to double the unit cell volume by doubling the *a*-axis. The crystal symmetry was removed, reducing the overall symmetry from the space group *Pnma* with cell parameters $a = 5.0280$ Å, $b = 10.3070$ Å, $c = 17.4020$ Å, $\alpha = 90.00°$, $\beta = 90.00°$, $\gamma = 90.00°$, and $Z = 6$ to the nominal space group *P*1, with cell parameters $a = 10.1160$ Å, $b = 10.3070$ Å, $c = 17.4020$ Å, $\alpha = 90.00°$, $\beta = 90.00°$, $\gamma = 90.00°$, and $Z = 1$.

**Table 2.** Tetrahedral M−O Bond Lengths from the Optimized Atomic Positions with $MoO_4$ Tetrahedra Surrounding the Cation Vacancies (Model **II**)

| atom | bond length (Å) | atom | bond length (Å) | atom | bond length (Å) | atom | bond length (Å) |
|---|---|---|---|---|---|---|---|
| Mo(1) | 1.8482 | Mo(2) | 1.8536 | Mo(3) | 1.8536 | Mo(4) | 1.8482 |
| | 1.8126 | | 1.7928 | | 1.7928 | | 1.8126 |
| | 1.8126 | | 1.7928 | | 1.7928 | | 1.8126 |
| | 1.7365 | | 1.7541 | | 1.7541 | | 1.7365 |
| Mo(5) | 1.7958 | Mo(6) | 1.7958 | Mo(7) | 1.8189 | Mo(8) | 1.8189 |
| | 1.7542 | | 1.7542 | | 1.7356 | | 1.7356 |
| | 1.8001 | | 1.8001 | | 1.8217 | | 1.8217 |
| | 1.8288 | | 1.8288 | | 1.8268 | | 1.8268 |
| Mo(9) | 1.8189 | Mo(10) | 1.8189 | Mo(11) | 1.7958 | Mo(12) | 1.7958 |
| | 1.7356 | | 1.7356 | | 1.7542 | | 1.7542 |
| | 1.8217 | | 1.8217 | | 1.8001 | | 1.8001 |
| | 1.8268 | | 1.8268 | | 1.8288 | | 1.8288 |
| V(1) | 1.7703 | V(2) | 1.7625 | V(3) | 1.7625 | V(4) | 1.7703 |
| | 1.7220 | | 1.7440 | | 1.7440 | | 1.7220 |
| | 1.7220 | | 1.7440 | | 1.7440 | | 1.7220 |
| | 1.7319 | | 1.7116 | | 1.7116 | | 1.7319 |
| V(5) | 1.7509 | V(6) | 1.7509 | V(7) | 1.7242 | V(8) | 1.7242 |
| | 1.7111 | | 1.7111 | | 1.7324 | | 1.7324 |
| | 1.7466 | | 1.7466 | | 1.7238 | | 1.7238 |
| | 1.7431 | | 1.7431 | | 1.7507 | | 1.7507 |
| V(9) | 1.7242 | V(10) | 1.7242 | V(11) | 1.7509 | V(12) | 1.7509 |
| | 1.7324 | | 1.7324 | | 1.7111 | | 1.7111 |
| | 1.7238 | | 1.7238 | | 1.7466 | | 1.7466 |
| | 1.7507 | | 1.7507 | | 1.7431 | | 1.7431 |

The fractional coordinates from the crystal structure were used for the initial atomic positions, which was geometry optimized with the new atomic designations. The optimized tetrahedral bond lengths for **II** and **III** are listed in Tables 2 and 3, respectively. When $MoO_4$ tetrahedra are placed around the vacancies (**II**), they consist of one short Mo−O bond (1.73−1.75 Å), corresponding to the displacement of the undercoordinated oxygen toward the $Mo^{6+}$ cation, one long Mo−O bond (1.83−1.85 Å), and two identical medium Mo−O bonds (1.79−1.82 Å). Conversely, the $VO_4$ tetrahedra are much more regular, with bond lengths of 1.71−1.77 Å, because they do not border the cation vacancies. Likewise, when $VO_4$ tetrahedra are placed around the vacancies (**III**), they consist of one short V−O bond (1.65−1.67 Å), one or two long V−O bonds (1.77−1.80 Å), and one or two medium V−O bonds (1.72−1.77 Å). The Mo−O bond

**Table 3.** Tetrahedral M−O Bond Lengths from the Optimized Atomic Positions with $VO_4$ Tetrahedra Surrounding the Cation Vacancies (Model **III**)

| atom | bond length (Å) | atom | bond length (Å) | atom | bond length (Å) | atom | bond length (Å) |
|---|---|---|---|---|---|---|---|
| Mo(1) | 1.8290 | Mo(2) | 1.8386 | Mo(3) | 1.8386 | Mo(4) | 1.8290 |
| | 1.8198 | | 1.7824 | | 1.7824 | | 1.8199 |
| | 1.8195 | | 1.7826 | | 1.7827 | | 1.8195 |
| | 1.7903 | | 1.7894 | | 1.7896 | | 1.7903 |
| Mo(5) | 1.7796 | Mo(6) | 1.7791 | Mo(7) | 1.8198 | Mo(8) | 1.8188 |
| | 1.7944 | | 1.7941 | | 1.7933 | | 1.7934 |
| | 1.7866 | | 1.7868 | | 1.8238 | | 1.8248 |
| | 1.8188 | | 1.8187 | | 1.8040 | | 1.8041 |
| Mo(9) | 1.8197 | Mo(10) | 1.8188 | Mo(11) | 1.7796 | Mo(12) | 1.7792 |
| | 1.7933 | | 1.7934 | | 1.7944 | | 1.7942 |
| | 1.8239 | | 1.8247 | | 1.7867 | | 1.7867 |
| | 1.8039 | | 1.8041 | | 1.8188 | | 1.8187 |
| V(1) | 1.8025 | V(2) | 1.7705 | V(3) | 1.7704 | V(4) | 1.8027 |
| | 1.7192 | | 1.7722 | | 1.7722 | | 1.7192 |
| | 1.7190 | | 1.7694 | | 1.7696 | | 1.7191 |
| | 1.6667 | | 1.6531 | | 1.6530 | | 1.6665 |
| V(5) | 1.7793 | V(6) | 1.7766 | V(7) | 1.7295 | V(8) | 1.7292 |
| | 1.6523 | | 1.6525 | | 1.6656 | | 1.6658 |
| | 1.7749 | | 1.7771 | | 1.7238 | | 1.7242 |
| | 1.7491 | | 1.7493 | | 1.7748 | | 1.7747 |
| V(9) | 1.7294 | V(10) | 1.7292 | V(11) | 1.7792 | V(12) | 1.7765 |
| | 1.6655 | | 1.6658 | | 1.6523 | | 1.6525 |
| | 1.7239 | | 1.7242 | | 1.7748 | | 1.7770 |
| | 1.7748 | | 1.7748 | | 1.7748 | | 1.7492 |

lengths for **III** are 1.78−1.84 Å. It should be noted that in the crystal structure, the disordered tetrahedra deviate from tetrahedral symmetry, distorting to $C_s$ symmetry with one short, two medium, and one long metal−oxygen bond length. However, in **III**, when vanadium is around the vacancy, several of the $VO_4$ tetrahedra (V(5), V(6), V(12)) have one short, one medium, and two long V−O bond lengths. In **II**, the Mo−O bonds of each tetrahedron are more reflective of what is seen in the crystal structure.

**Simulated Raman Spectrum.** The results of the simulated Raman spectra are compared with the experimental spectrum in Table 4 and Figure 3. Because the simulations do not give intensities, the peak positions from the calculated spectra are shown as lines with the same height. There is good agreement in terms of band positions between the spectra, and all of the calculated bands can be assigned to the experimental bands. Of particular interest is the observed band located at 1016 $cm^{-1}$. When cation vacancies are not included in the model, the band is missing. However, when vacancies are used in the model, a band appears in the range from 979 to 1019 $cm^{-1}$ for model **II** and from 969 to 1006 $cm^{-1}$ for model **III**, demonstrating that the observed band at 1016 $cm^{-1}$ is associated with transition metal−oxygen bonds adjacent to the cation vacancies. The current theoretical work combined with previous experimental results[7] that excluded the assignment of the band at 1016 $cm^{-1}$ to V═O demonstrate that the band appearing at 1016 $cm^{-1}$ should be attributed to the shortest Mo═O bonds (1.73−1.75 Å) that border cation vacancies. In addition, The DMol3 calculations predict model **II** to be significantly more stable than model **III**, the binding energy of the former being lower by 60.5 kcal $mol^{-1}$. This corroborates the finding that model **II** is a better representation of the experimental structure.

The fact that two-coordinate oxygen atoms (i.e., Mo═O−Mg) in $MoO_4$ tetrahedra produce the Raman band above 1000 $cm^{-1}$ is notable because the presence of a high-frequency band has been taken as evidence for the presence of the one-coordinated oxygen atoms in M═O bonds. Examples of other metal oxides that support the assignment are $Al_2(MoO_4)_3$, $KAl(MoO_4)_2$, and $Fe_2(MoO_4)_3$. These materials exhibit Mo═O Raman bands at 1027, 1003, and 1000 $cm^{-1}$, respectively,[27−30] and the oxygen atoms of the $MoO_4$ tetrahedra in the three compounds are two coordinate (i.e., Mo═O−Al, Mo═O−Fe).[31−33] In addition, $Al_2(WO_4)_3$ and $MgV_2O_5$ exhibit W═O and V═O stretching vibrations at 1051 and 1002 $cm^{-1}$, respectively,[34,35] while the oxygen atoms in the $WO_4$ tetrahedra and $VO_5$ pyramids are two-coordinate[36,37] (i.e., W═O−Al and V═O−Mg). Thus, Raman bands above 1000 $cm^{-1}$ can be attributed to the stretching vibrations of $MO_4$ tetrahedra and $MO_5$ pyramids from either two-coordinate oxygen atoms or one-coordinate oxygen atoms.

**Two Variables Affecting the M−O Stretching Frequencies of $MO_4$ Tetrahedra (M = V, Mo, W).** An empirical correlation between bond length and Raman frequency based on the diatomic approximation by Wachs and co-workers has been used to estimate both V−O and Mo−O bond lengths from the Raman frequencies.[25,26] According to the correlation, the Raman band occurring at 1016 $cm^{-1}$ should be assigned to either ∼1.59 Å V−O bonds or ∼1.68 Å Mo−O bonds. These short bond lengths are not observed in the crystallographic model nor are they observed in the geometry-optimized model. Since the correlation includes only a single variable, it is simple to use, but it is important to recognize its limitations. For example, both the $\beta$-$Bi_2Mo_2O_9$ and $FeClMoO_4$ have exactly the same Mo−O bond length of 1.756 Å in their $MoO_4$ tetrahedra but show very different highest Raman frequencies at 887 and 975 $cm^{-1}$, respectively, while the correlation predicts a single, identical frequency at 863 $cm^{-1}$.[26]

The Mo−O stretching vibrations blue-shift with either a higher degree of tetrahedral angular distortion or with shorter Mo−O bond lengths as described previously.[7] A higher $MoO_4$ tetrahedral angular distortion combined with a longer


(27) Knoezinger, H.; Jeziorowski, H. *J. Phys. Chem.* **1978**, *82*, 2002−2005.
(28) Maczka, M.; Hermanowicz, K.; Tomaszewski, P. E.; Hanuza, J. *J. Phys. Condens. Matter* **2004**, *16*, 3319−3328.
(29) Maczka, M.; Kojima, S.; Hanuza, J. *J. Raman Spectrosc.* **1999**, *30*, 339−345.
(30) Forzatti, P.; Mari, C. M.; Villa, P. *Mater Res. Bull.* **1987**, *22*, 1593−1602.
(31) Harrison, W. T. A. *Mater Res. Bull.* **1995**, *30*, 1325−1331.
(32) Harrison, W. T. A.; Cheetham, A. K.; Faber, J., Jr. *J. Solid State Chem.* **1988**, *76*, 328−333.
(33) Chen, H. *Mater Res. Bull.* **1979**, *14*, 1583−1590.
(34) Maczka, M.; Paraguassu, W.; Souza Filho, A. G.; Freire, P. T. C.; Mendes Filho, J.; Melo, F. E. A.; Hanuza, J. *J. Solid State Chem.* **2004**, *177*, 2002−2006.
(35) Popovic, Z. V.; Konstantinovic, M. J.; Gajic, R.; Popov, V. N.; Isobe, M.; Ueda, Y.; Moshchalkov, V. V. *Phys. Rev. B.: Condens. Matter Mater Phys.* **2002**, *65*, 184303/1−184303/8.
(36) Craig, D. C.; Stephenson, N. C. *Acta Crystallogr., Sect. B.* **1968**, *24*, 1250−1255.
(37) Onoda, M.; Ohyama, A. *J. Phys. Condens. Matter* **1998**, *10*, 1229−1236.

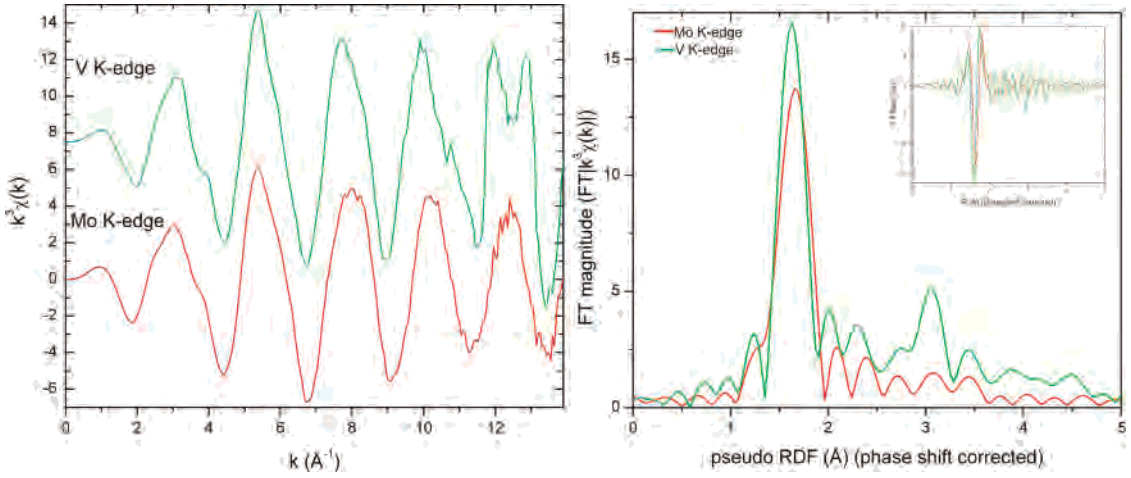


**Figure 4.** Mo and V K-edge EXAFS spectra of $Mg_{2.5}VMoO_8$. Spectra were measured at room temperature in transmission geometry.

**Table 4.** Assignments and Raman Shifts ($cm^{-1}$) in $Mg_{2.5}VMoO_8$

| mode | | exptl | calcd without vacancies (**I**) | calcd with Mo−O around vacancies (**II**) | calcd with V−O around vacancies (**III**) |
|---|---|---|---|---|---|
| bending | $MoO_4$ | 326, 370 | 321−372 (345) | 310−375 (345) | 312−379 (346) |
| | $VO_4$ | 387 | 380−396 (388) | 380−430 (405) | 382−428 (405) |
| asymmetric stretching | $MoO_4$ | 823 | 702−799 (750) | 731−799 (765) | 736−796 (766) |
| | $VO_4$ | 791 | | | |
| symmetric stretching | $MoO_4$ | 910 | 929−932 (930) | 909−965 (937) | 918−952 (935) |
| | $VO_4$ | 860 | 832−867 (850) | 804−897 (850) | 810−898 (854) |
| symmetric stretching | $MoO_4$ | 1016 | missing | 979−1019 | |
| M═O−Mg stretching | $VO_4$ | 944 | missing | | 969−1006 |

Mo−O bond length or a lower $MoO_4$ tetrahedral angular distortion combined with a shorter Mo−O bond length can produce high-frequency Mo−O stretching vibrations. The difference between the two frequencies in $\beta$-$Bi_2Mo_2O_9$ and $FeClMoO_4$ and the deviation from the predicted value of 863 $cm^{-1}$ result from changes in the degree of angular distortion in the $MoO_4$ tetrahedra for the $\beta$-$Bi_2Mo_2O_9$ (slightly distorted) and $FeClMoO_4$ (highly distorted) structures.

The two key variables, M−O bond length and tetrahedral angular distortion, for $MO_4$ (M = Mo, V) obtained by the geometry optimization were compared with those obtained by crystallography. The shortest Mo−O length (1.73−1.75 Å) for model **II** obtained by the geometry optimization is slightly longer than the shortest Mo−O bond length of 1.70 Å obtained by the crystallographic result.[5,7,8] However, the $MoO_4$ tetrahedra for model **II** that border vacancies have a higher degree of angular distortion than that observed from the crystallographic data.[5] Consequently, the simulated Raman frequencies obtained from the geometry-optimized atomic positions for model **II** are seen to be consistent with empirical observations when both bond lengths and angular distortion are considered.

**X-ray Absorption Spectroscopy.** To further examine the validity of model **II** in describing the local structure of $Mg_{2.5}VMoO_8$, EXAFS was used to probe the local coordination environments surrounding the $V^{5+}$ and $Mo^{6+}$ cations. The room-temperature Mo and V K-edge EXAFS spectra of $Mg_{2.5}VMoO_8$ and their corresponding Fourier transforms are presented in Figure 4. The EXAFS spectra measured at the Mo and V K-edges are similar, with major spectral differences at $k \approx 11$ and 12−13 $Å^{-1}$. The corresponding Fourier-transformed EXAFS spectra reveal major differences in the positions and amplitudes of the first coordination shells, centered around 1.6−1.8 Å, as well as significant amplitude differences at ~3.2 Å. Specifically, the first Mo−O shell in the Mo K-edge spectrum is lower in amplitude and centered at a greater radial distance than the first shell in the V K-edge spectrum. Qualitatively, differences in heights and peak positions of metal−oxygen shells between two spectra indicate that the Mo−O and V−O average bond lengths and distributions are different. Furthermore, a greater amplitude in the V K-edge spectrum at radial distance $R \approx 3.2$ Å than that observed in the Mo K-edge spectrum may indicate that a greater number of backscattering atoms surround V cations than Mo cations, consistent with model **II**. The Mo and V K-edge spectra were fit up to 4 Å with all Mo/V−O and Mo/V−Mg SS paths, generated by binning bond lengths from models **II** and **III** (Figure 5b and e). Model **II** fit the EXAFS spectra better ($R = 0.037$, $\chi^2 = 7190$) than model **III** ($R = 0.144$, $\chi^2 = 72726$). Despite reasonable fits of models **II** and **III** to Mo and V K-edge spectra, $\Delta E_0$ values were significantly greater than 10 eV in all cases (See Table S2). It is reasonable to suspect that fitting amplitude differences at $R > 3.0$ Å with models **II** and **III** converged to a local minimum and may not provide a unique solution because of the large number of O and Mg atoms with very similar distances, in the range of $R \approx 3.0$−3.5 Å (Figure S1). In model **II**, four additional Mg atoms surround each V cation (96 in total) than surround Mo cations (84 Mg atoms); each one of the four $Mg^{2+}$ cations has a unique scattering distance. In model **III**, the situation is reversed with four more $Mg^{2+}$ atoms surrounding each Mo than

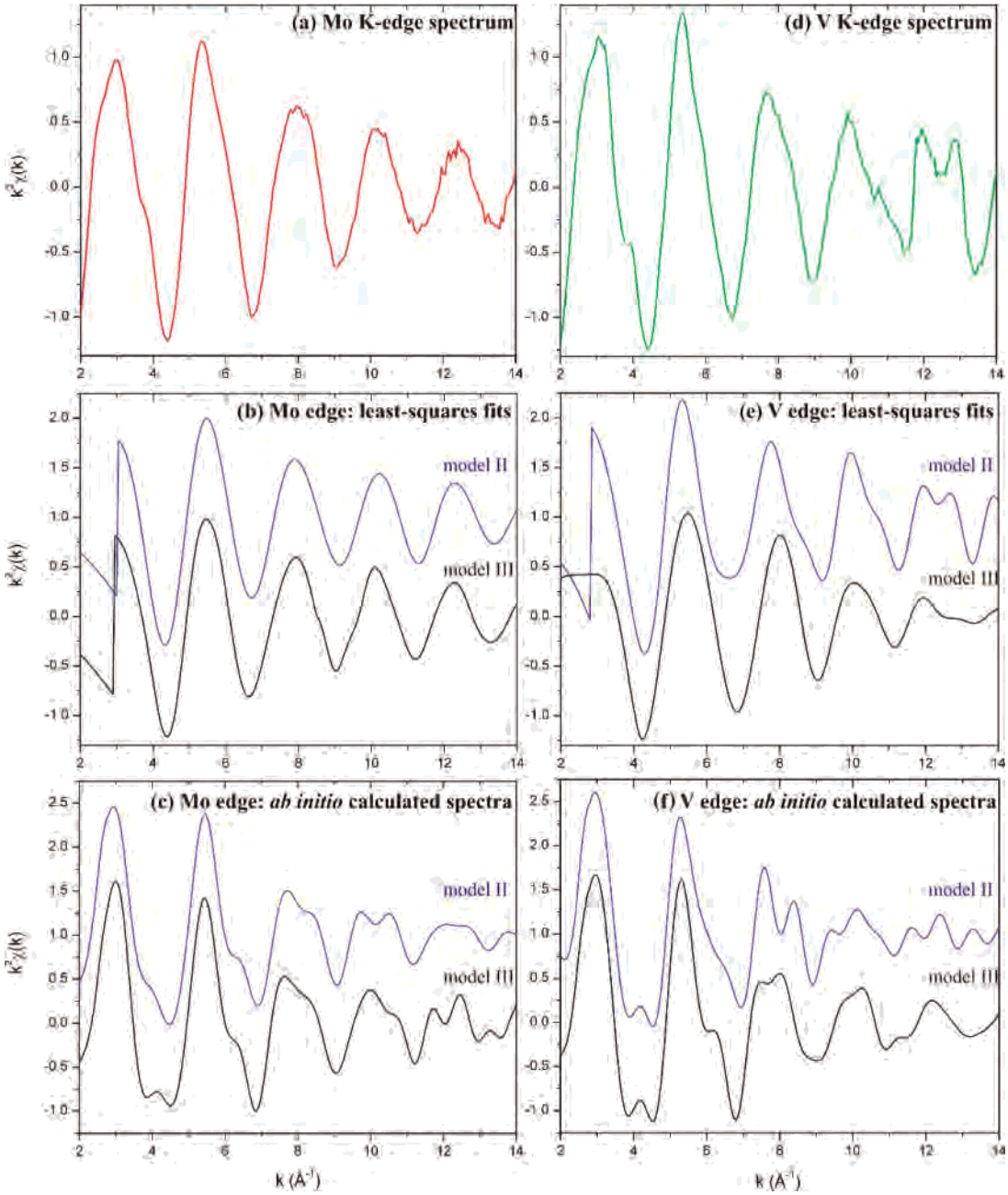


**Figure 5.** (a) $Mg_{2.5}VMoO_8$ Mo K-edge EXAFS spectrum. (b) Least-squares fits of models **II** and **III** to the Mo K-edge EXAFS spectrum. (c) Mo K-edge EXAFS spectrum calculated ab initio from geometry-optimized models **II** and **III**. (d) $Mg_{2.5}VMoO_8$ V K-edge EXAFS spectrum. (e) Least-squares fits of models **II** and **III** to the V K-edge EXAFS spectrum. (f) V K-edge EXAFS spectrum calculated ab initio from geometry-optimized models **II** and **III**.

surround each V; each has a unique scattering distance. Additionally, significant numbers of oxygen atoms are also present in $3.2 \leq R \leq 3.5$ Å and may obscure analysis of $Mg^{2+}$ back-scatterers.

In addition to least-squares fits of Mo and V K-edge spectra, the EXAFS at each edge was calculated ab initio for models **II** and **III**. Spectra were calculated from each of 12 Mo and 12 V sites and summed (Figure 5c and 5f). From the ab initio calculations, it is evident that model **II** qualitatively reproduces the Mo and V K-edge spectra better than the spectra calculated from model **III**. Together with qualitative support for model **II** from least-squares fits of binned SS paths, qualitative agreement of model **II** from ab initio calculations of geometry optimized models provides strong evidence for clustering of $Mo^{6+}$ cations around $Mg^{2+}$ cation vacancies. Because of the aforementioned difficulties in fitting $R > 3.0$ Å, quantitative analyses of $Mg_{2.5}VMoO_8$ EXAFS spectra at the Mo and V K-edges were limited to fitting models **I**, **II**, and **III** to the first metal oxygen shells.

Least-squares fits of geometry-optimized models to the first shell in the Fourier-transformed spectra are presented in Figure 6, along with corresponding histograms that depict bond length distributions and populations. Detailed fit results using **I**, **II**, and **III** are presented in Table 5. Metal−oxygen bond distances and distributions calculated from **II** fit the Mo−O and V−O shells better than models **I** and **III**, with a total misfit of $R_{tot} = 3.5\%$, where $R_{tot} = (R_{Mo-O} + R_{V-O})/2$. In comparison, simultaneous fits of Mo and V K-edge

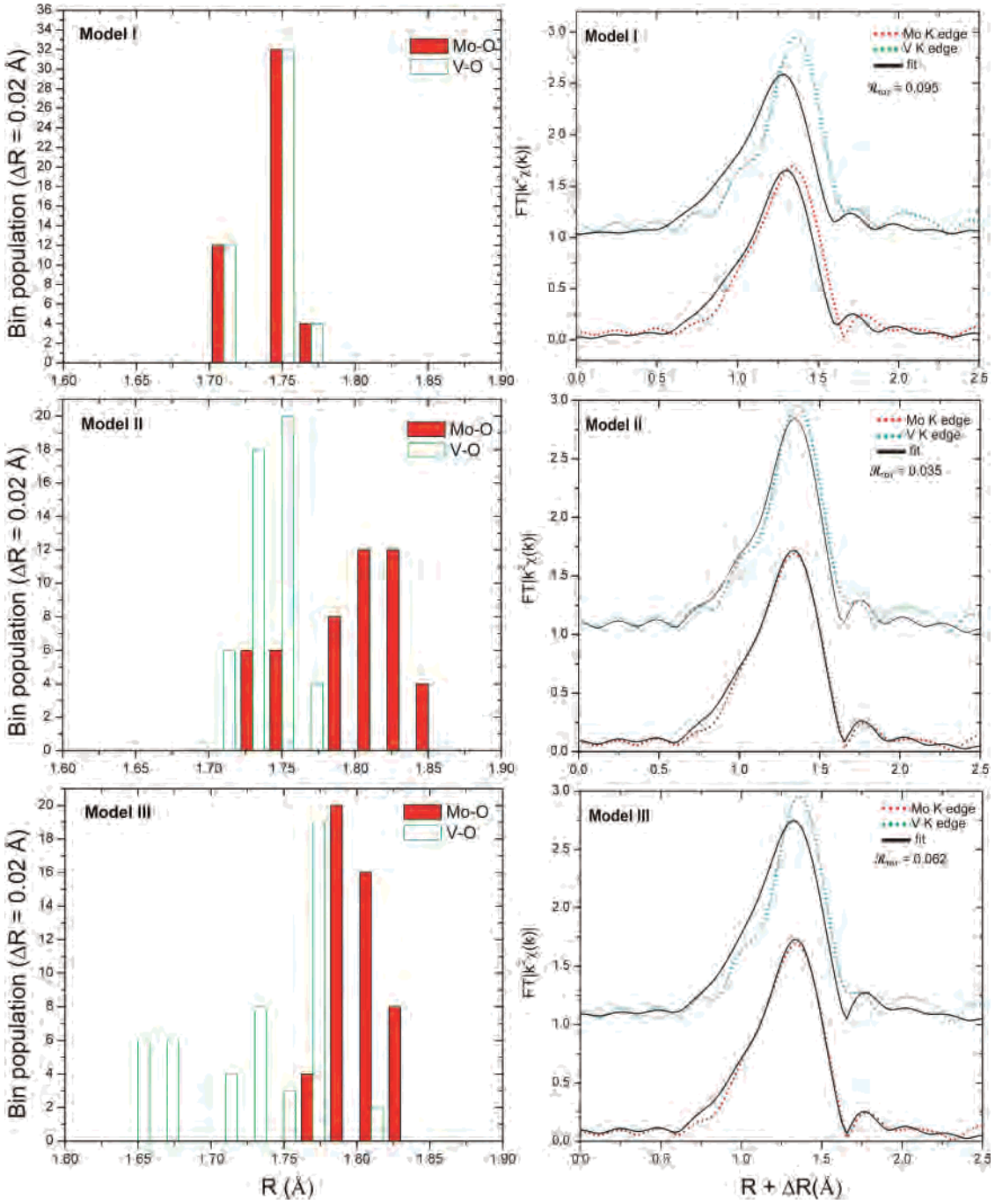


**Figure 6.** Least-squares fits of models **I**, **II**, and **III** to Mo and V K-edge EXAFS spectra of $Mg_{2.5}VMoO_8$. Histograms (left panel) were calculated by division of geometry optimized Mo−O and V−O bond distances into 0.02 Å bins and (right panel) results from simultaneous least-squares fits of models **I**, **II**, and **III** to Fourier-transformed Mo and V K-edge spectra of $Mg_{2.5}VMoO_8$.

spectra with model **I** converged with $R_{tot} = 9.5\%$, and model **III** converged with $R_{tot} = 6.2\%$.

Examination of histograms in Figure 6, generated from division of geometry-optimized bond lengths into 0.02 Å bins, illustrates the distributions of Mo−O and V−O bond distances in $MoO_4$ and $VO_4$ tetrahedra, respectively. In model **I**, the Mo−O and V−O coordination environments and distributions are identical (Table 1 and Figure 5) because of the crystallographic disorder of $Mo^{6+}$ and $V^{5+}$ cations. A significant misfit of **I** to the EXAFS spectra demonstrates that the Mo−O and V−O bond distributions and local coordination environments are different. Differences between respective Mo−O and V−O bond lengths were not evidenced in structure determination by single-crystal X-ray diffraction[5] or neutron diffraction[24] because of crystallographic disorder that arises from the isolated nature of hexagonal channels within the $Mg_{2.5}VMoO_8$ structure. In **II**, the distribution of Mo−O bond lengths in the $MoO_4$ tetrahedra is broader than that of V−O bonds in $VO_4$ tetrahedra. Conversely, in **III**, the distribution of V−O bond lengths in $VO_4$ tetrahedra is greater than the distribution of Mo−O bond lengths in the $MoO_4$ tetrahedra (Figure 5). Model **II** fits the Mo−O and V−O shells statistically better than Models **I** and **III** (Figure 5 and Table 1). This result indicates that $VO_4$

**Table 5.** XAS Least-Squares Fit Results

| | $R$ | red. $\chi^2$ | $\Delta E_0$ (eV) | $\Delta R$ (Å)[a] | $\sigma^2$ (Å$^2$) | $S_0^{2}$[b] |
|---|---|---|---|---|---|---|
| model **I** | 0.095 | 1022 | | | | |
| Mo−O | 0.090 | | −8 (3) | 0.004 (12) | 0.002 (20) | 0.96 |
| V−O | 0.110 | | -6 (5) | 0.004 (12) | 0.001 (2) | 0.81 |
| model **II** | 0.035 | 421 | | | | |
| Mo−O | 0.008 | | −1 (3) | −0.016 (8) | 0.0002 (10) | 0.96 |
| V−O | 0.062 | | −1 (3) | −0.016 (8) | 0.0001 (10) | 0.81 |
| model **III** | 0.062 | 752 | | | | |
| Mo−O | 0.009 | | −1 (5) | −0.02 (1) | 0.001 (1) | 0.96 |
| V−O | 0.115 | | −1 (4) | −0.02 (1) | 0.00002 (100) | 0.81 |

[a] Bond distances were derived from the geometry-optimized structural models of $Mg_{2.5}VMoO_8$. [b] $S_0^2$ for Mo and V spectra were set to values determined from fits of $MgMoO_4$ and $Mg_3(VO_4)_2$ reference spectra, measured at 10, 100, 200, and 300 K.

tetrahedra have higher symmetry than the distorted $MoO_4$ tetrahedra and is consistent with the successful simulation of vibrational frequencies to match the experimental Raman spectrum of $Mg_{2.5}VMoO_8$.

## Conclusion

Raman spectra of complex oxides can be simulated accurately by quantum mechanical simulations. The geometry-optimized structures, simulated Raman spectra of $Mg_{2.5}VMoO_8$, and analysis by EXAFS spectroscopy provide strong evidence that $MoO_4$ has much higher degree of tetrahedral angular distortion than $VO_4$ in the crystalline $Mg_{2.5}VMoO_8$ structure and that cation vacancies can cause high-frequency vibrational Raman bands, similar to surface terminal V═O, Mo═O, and W═O double bonds where oxygen atoms are one-coordinate. Furthermore, the observed band at 1016 $cm^{-1}$ is likely attributed to the Mo−O stretching of two coordinate oxygen (one bond to $Mg^{2+}$ and one bond to $Mo^{6+}$) that border the cation vacancies.

**Acknowledgment.** We gratefully acknowledge the support from the National Science Foundation (Solid-State Chemistry Awards DMR-0312136 and DMR-0604454), the EMSI program of the National Science Foundation at the Northwestern University Institute for Environmental Catalysis (Grant 98103778), and the Department of Energy BES-Chemical Sciences, Geosciences, and Biosciences Division under Grant DE-FG0203ER15457 and the use of the central facilities supported by the MRSEC program of the National Science Foundation (DMR-0520513) at the Materials Research Center of Northwestern University.

**Supporting Information Available:** Detailed analysis of EXAFS spectra with models **II** and **III** histograms and least-squares fit. This material is available free of charge via the Internet at http://pubs.acs.org.

IC7006815